Nanoscale

COMMUNICATION

View Article Online
View Journal | View Issue

Cite this: *Nanoscale*, 2017, **9**, 1398

Received 26th October 2016,
Accepted 19th December 2016

DOI: 10.1039/c6nr08387k

www.rsc.org/nanoscale

Facile three-dimensional nanoarchitecturing of double-bent gold strips on roll-to-roll nanoimprinted transparent nanogratings for flexible and scalable plasmonic sensors†

Jung-Sub Wi,[a] Seungjo Lee,[b] Sung Ho Lee,[c] Dong Kyo Oh,[b] Kyu-Tae Lee,[d] Inkyu Park,[e] Moon Kyu Kwak*[c] and Jong G. Ok*[b]

We develop scalable 3D plasmonic nanoarchitectures comprising a double-bent nanoscale Au strip array integrated within the transparent nanograting framework, which can be continuously fabricated on a large-area flexible substrate *via* roll-to-roll nanoimprint lithography and angled Au deposition, realizing localized surface plasmon resonance with higher sensitivity in a smaller footprint.

Localized surface plasmon resonance (LSPR), leading to optical absorption peaks at specific wavelengths due to surface plasmon confinement in a nanoscale metallic structure, has been capitalized in many diverse sensing devices.[1,2] For achieving clean and narrow resonance peaks that are crucial for making highly sensitive and reliable LSPR-based sensors, fabrication of uniform plasmonic nanostructures is required. A bottom-up approach, typically relying on colloidal nanoparticle synthesis, affords uniform shape and narrow size distribution, yet demands positioning and configuration of the particles into the targeted device structure on a wafer-scale substrate, along with exacting alignment especially for anisotropic nanoparticles.[3,4] Top-down nanofabrication techniques involving lithography and etching can be used to directly shape the three-dimensional (3D) LSPR structures on a substrate,[5–9] but are often limited by complex procedures, substrate materials, processable areas, and high cost for further practical applications. Hence, a simple, cost-effective, and universal methodology to create 3D plasmonic nanostructures on various flexible and transparent substrates, without resorting to tedious nanoscale manipulation as well as additional steps of metal lift-off or chemical/physical etching, is called for.

One facile route for creating the discrete metallic LSPR nanoarchitecture, particularly aiming for high refractive index sensitivity and fabrication throughput, is to first form a polymeric nanograting pattern array and then deposit a metal layer onto the top and/or sidewall of each grating. Here, the long metallic structures can be 'folded' along the nanograting topography in a more compact fashion, compared to the ones simply patterned on a flat surface, thereby yielding the longer oscillation length for surface plasmon polaritons (SPPs) for higher sensitivity in a smaller device footprint.

In this regard, nanoimprint lithography (NIL)[10,11] can provide an attractive solution to mechanically stamp the transparent nanograting structure on any desired substrates such as flexible and transparent polymers, without the aid of complicated optical lithography and additional etching processes. NIL accompanied by subsequent angled metal deposition enables high-throughput and low-cost 3D LSPR nanoarchitecturing with high reproducibility, compared to the commonly used electron-beam lithography where each metallic pattern should be defined one by one for prohibitive time and cost. Moving forward, roll-to-roll (R2R) NIL can further extend the scalability and fabrication speed by conducting NIL in a manner of continuous rolling.[12–14] In R2R NIL, a flexible imprinting mold (stamp) is first wrapped around a cylindrical roll which then continuously stamps the desired pattern on the target substrate typically coated with a UV-curable polymer resin, as the rolling proceeds under a conformal contact and with UV curing at the outlet.

In this work, we develop a facile, high-throughput, and potentially more scalable methodology to create transparent and flexible 3D LSPR nanoarchitectures integrated within the R2R NIL-ed polymer nanograting framework. We conduct angled gold (Au) deposition to form discretized Au strips in the way to be bent along the morphology of each nanograting, readily architecturing the 3D LSPR structure without litho-

[a]*Center for Nano-Bio Measurement, Korea Research Institute of Standards and Science, Daejeon 34113, Korea*
[b]*Department of Mechanical and Automotive Engineering, Seoul National University of Science and Technology, Seoul 01811, Korea. E-mail: jgok@seoultech.ac.kr*
[c]*School of Mechanical Engineering, Kyungpook National University, Daegu 41566, Korea. E-mail: mkkwak@knu.ac.kr*
[d]*Department of Materials Science and Engineering, University of Illinois at Urbana-Champaign, Urbana, Illinois 61801, USA*
[e]*School of Mechanical and Aerospace Engineering, KAIST, Daejeon 34141, Korea*

†Electronic supplementary information (ESI) available: Fabrication detail, electromagnetic simulation and absorbance spectra of the Au strips. See DOI: 10.1039/c6nr08387k

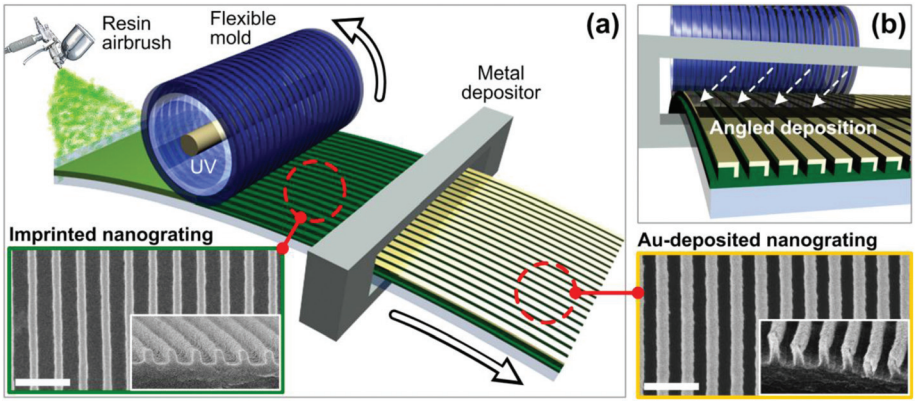

Fig. 1 (a) Schematic and conceptual drawing of the overall fabrication procedure based on continuous R2R NIL, beginning from airbrushing-based resin coating to metal evaporation. (b) Enlarged conceptual view of angled Au evaporation over the NIL-ed transparent polymer nanograting structures. Exemplified SEM images before and after Au evaporation are also indicated. The scale bars represent 500 nm.

graphy and etching. We explore the correlation between the bent shape of Au strips depending on the deposition angle and the plasmonic sensing performance, and further investigate the contribution of each linear fragment of the bent Au strip to the overall LSPR characteristics. Many practical applications can benefit from the developed method as it can make more compact LSPR nanoarchitectures on any desired substrates at high speed and low cost. As one specific example, we demonstrate that the structure fabricated on a flexible large-area substrate can work as a transparent biomolecular sensor.

Fig. 1 depicts the overall fabrication scheme. Briefly, the transparent nanograting structure is created on a flexible substrate *via* R2R NIL, followed by angled Au deposition. By using a flexible polydimethylsiloxane (PDMS) mold carrying the 200 nm-period (1 : 1 duty) and 100 nm-high nanograting pattern, R2R NIL was performed onto the polyurethane acrylate (PUA)-coated polyethylene terephthalate (PET) substrate. Here the PUA film was coated by airbrushing to ensure continuous and controlled coating, which is well-suited for R2R NIL.[15] The other detailed R2R NIL conditions can be found elsewhere.[13] After R2R NIL is done, the Au strips were thermally evaporated (30 nm nominal thickness) at three different oblique angles (5°, 35°, and 50°) on the PUA nanogratings. Further fabrication details are described in the ESI.† The representative scanning electron microscopy (SEM) images of top and cross-sectional views of the nanograting patterns before and after angled Au deposition are also shown in Fig. 1.

Fig. 2a–c further demonstrate the SEM images of the planar views of three cases with varied Au deposition angles. For the case of the deposition angle of 5°, the Au strips were deposited on both the top and bottom surfaces of the gratings. Although the top surfaces of the gratings were fully covered by Au, the tilted deposition and the consequent shadowing effect resulted in narrow slits on the bottom surfaces where the Au flux could not reach. These slits at the bottom surfaces appeared as a dark contrast in Fig. 2a. By increasing the oblique angle of the Au flux from 5° to 35°, the dark contrast regions at the bottom surfaces were widened as shown in Fig. 2b, and simultaneously, the Au strips on the top and bottom surfaces of the gratings were connected by the Au films deposited on the sidewall surfaces as illustrated in the inset of Fig. 2b. When the deposition angle was further tilted to 50°, the Au flux could not reach the bottom surfaces, and the Au films were deposited at the top and a part of the sidewall surfaces (Fig. 2c).

The optical properties of the prepared Au strips on the gratings were investigated by measuring their absorbance curves with a spectrophotometer (UV-2600, Shimadzu, Japan). Unpolarized light was normally incident on the sample surfaces and the intensity of transmitted light was recorded at the back of the samples. Since the resonance conditions of plasmonic nanostructures depend on the refractive indices of surrounding materials, which is the working principle of the LSPR sensor, the absorbance spectra of the prepared samples were measured in air and in deionized water as shown in Fig. 2d–f. The absorbance curves in Fig. 2d, e and f were obtained from the samples in Fig. 2a, b and c, respectively. Among the three types of the Au strips, the double-bent Au strips (DAS) on the grating in Fig. 2b show the most sensitive response to the change of the surrounding medium. The shift of the LSPR peak of the DAS (Fig. 2d) is approximately 3 times larger than that of the single-bent Au strips as indicated in Fig. 2e and f. The refractive index sensitivity (spectral peak shift per refractive index unit) and its figure of merit (refractive index sensitivity per spectral width of the absorbance peak) of the DAS are evaluated to be about 210 nm RIU^{-1} and 4.2, respectively, as shown in the inset graph of Fig. 2(b). Although the sensing performance of the DAS is not superior to the records of the sensitivity and the figure of merit reported in the literature,[1–9,16–19] it is sufficiently high to be applicable in molecular sensing with femtogram-level sensitivity as demonstrated in the later part of this communication.

To understand the electromagnetic origin of the sensitive response of the DAS to the change of the surrounding medium, the extinction, absorption, and scattering cross

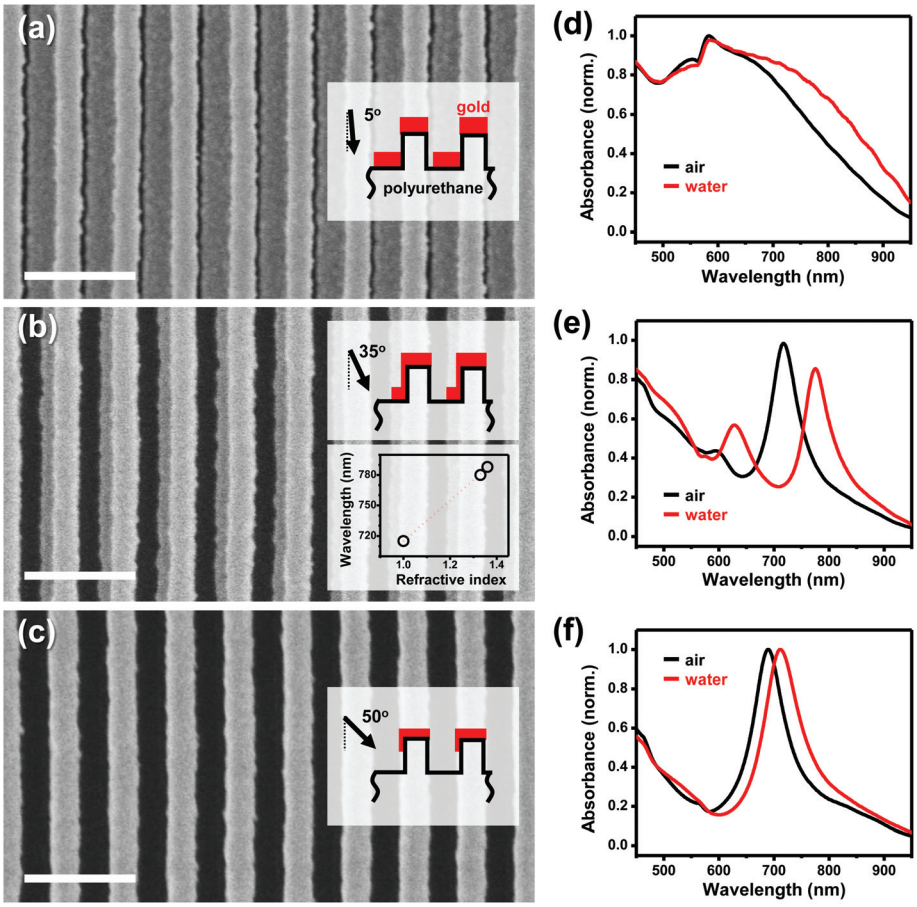

Fig. 2 (a–c) SEM images of the Au patterns deposited with oblique angles of (a) 5°, (b) 35°, and (c) 50° on the 1D polyurethane grating structures. The scale bars represent 400 nm. Insets are schematic illustrations of the cross-sectional views of the samples. (d–f) Measured absorbance curves of the Au strips: (d) from (a), (e) from (b), (f) from (c). Black and red curves of the samples were obtained in air and water, respectively. Inset graph in (b) shows the LSPR peak wavelengths measured in three different dielectric media (air, water and ethanol).

sections of the DAS (Fig. 3a) were calculated by using 2D finite difference time domain (FDTD) simulation software (Lumerical FDTD Solution 8.9). In the FDTD simulation, 20 nm-thick double-bent Au strips with a 90 nm-wide top, 40 nm-wide bottom, and 120 nm height were modeled as the DAS. The refractive index of the polyurethane nanograting was assumed to be 1.5. More details of the simulation model are described in the ESI.† The calculated spectra in Fig. 3a show the two characteristic peaks at the wavelengths of 560 nm and 810 nm, which originate from the absorption and scattering of incident light, respectively. Interestingly, internal segments of the DAS, such as the Au film on the top or bottom surface only, are activated with the light of around 560 nm wavelength, while they are not activated at a longer wavelength as shown in Fig. 3b. Moreover, the pair of Au strips at the top and bottom surface also shows a single absorbance peak (black colored curve in Fig. 3b). Its shape is almost identical to the sum of the absorbance peaks for non-interacting two Au strips on the top and bottom surface. Therefore, the simulation results in Fig. 3a and b demonstrate that the extinction peak at the wavelength of 810 nm is a specific characteristic of the DAS.

The charge distributions calculated at the cross-section of the DAS are useful to visualize the two interacting modes of the DAS with incident light. Under the exposure of 560 nm wavelength light, the top, sidewall, and bottom strips in the DAS work as individual dipoles as shown in the left-hand side image of Fig. 3c. Because the resonant wavelengths of the internal segments of the DAS are all close to 560 nm as demonstrated in Fig. 3b, it is reasonable that the dipole modes of each segment are activated. The corresponding electric field contours to visualize the local plasmonic field enhancement around the DAS are shown in the ESI (Fig. S1†). Under the exposure of 810 nm wavelength light, however, the DAS function as a single object as shown in the right-hand side image in Fig. 3c where a dipole with a long oscillation length of surface plasmon polaritons is generated at the interfacial plane between the DAS and the grating. Therefore, the simulation results in Fig. 3c clearly show that folding of the Au film into the shape of the DAS allows to provide the surface plasmon polaritons with a long oscillation length. Notably, a longer oscillation length of surface plasmon under a longer excitation wavelength is favorable for increasing the refractive index sensitivity.[19–21] It is also reported elsewhere that the refractive

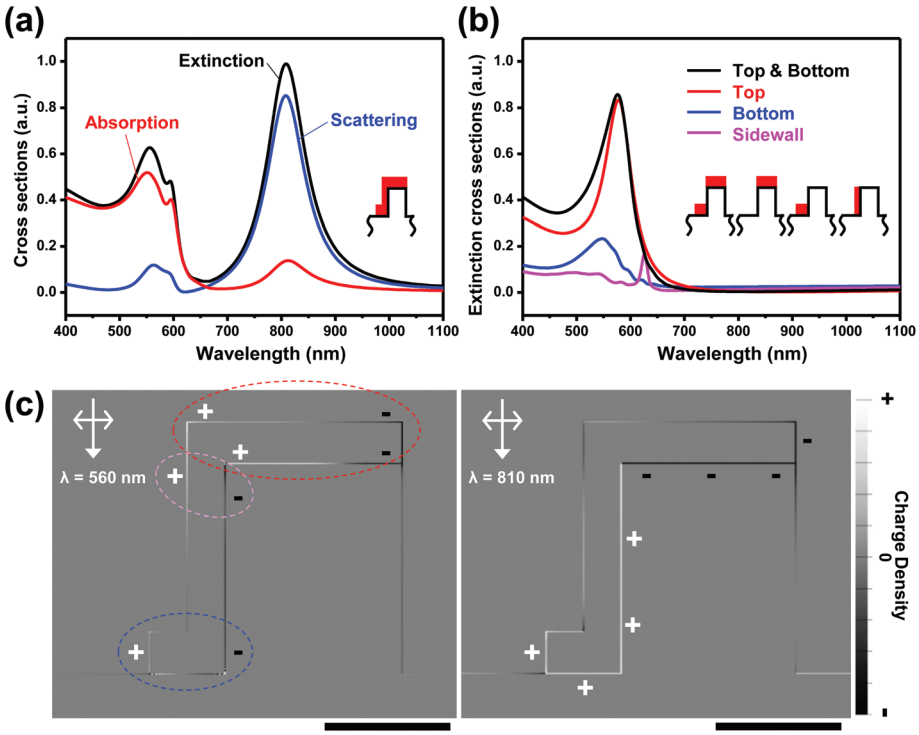

Fig. 3 (a) Calculated (black) extinction, (red) absorption, and (blue) scattering cross-sections of the double-bent Au strips on 1D grating. The periodic Au strips (periodicity = 200 nm) were modeled based on the SEM image in Fig. 2(b). (b) Calculated extinction cross-sections of the partial segments of the double-bent Au strips: (black) top and bottom planes, (red) top plane, (blue) bottom plane, and (pink) sidewall plane on the grating. (c) Calculated charge distribution monitored at the cross section of the double-bent Au strips. The wavelengths of the incident light were (left) 560 nm and (right) 810 nm. The scale bars represent 50 nm.

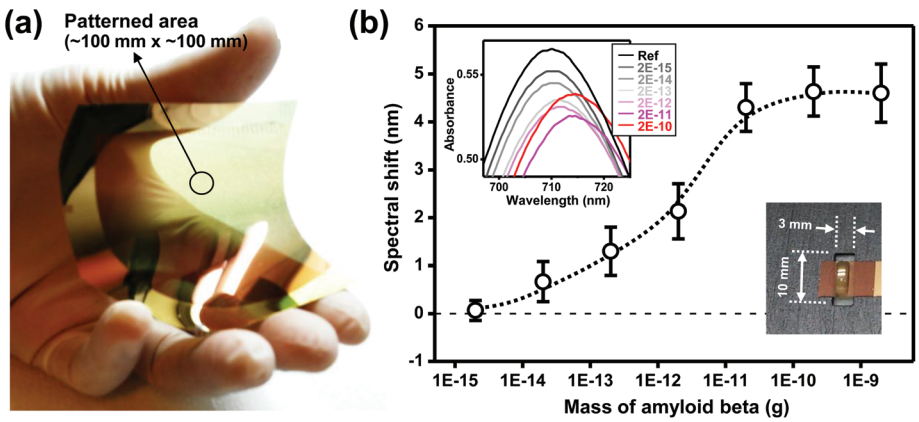

Fig. 4 (a) Photograph of flexible and semi-transparent DAS sensor. (b) Average LSPR peak shift of the DAS sensor treated with different concentrations of beta amyloid in deionized water. 2 μL drop of β-amyloid solution with concentrations of 10^{-9}, 10^{-8}, 10^{-7}, 10^{-6}, 10^{-5}, 10^{-4}, and 10^{-3} mg ml^{-1} was evaporated on the sensor surface. Inset graph and photograph show, respectively, the representative absorbance curves and the sample observed after dropping the beta amyloid solution.

index sensitivities of Au nanostructures increased linearly with their resonance wavelengths as long as the real part of the dielectric function of Au changed linearly with the incident light wavelength.[19] In our experiments, the increase in the Au deposition angle from 35° to 50° led to the decrease in the cross-sectional length of the Au strip. This induced a blue-shift of the resonant wavelength of Au strips, and also decreased their refractive index sensitivity (Fig. 2d, f and S3 in the ESI†).

Finally, the potential of the DAS as a LSPR-based optical sensor, which could be fabricated on a transparent and flexible substrate as shown in Fig. 4a, was evaluated with a β-amyloid peptide, one of the pathological biomarkers for Alzheimer's disease.[22,23] 2 μL drop of aqueous β-amyloid (amyloid beta 1-42 rat, Sigma-Aldrich) solution with concentrations of 10^{-9}, 10^{-8}, 10^{-7}, 10^{-6}, 10^{-5}, 10^{-4}, and 10^{-3} mg ml^{-1} was evaporated on the sensor surface. Non-volatile β-amyloid molecules left on

the DAS induced the refractive index change near the sensor surface and caused the spectral shift of the LSPR peak. The corresponding spectral shifts by varying the concentration of β-amyloid, are displayed in Fig. 3b. To plot these data, the mass of β-amyloid remaining on the DAS was calculated from the volume and concentration of the solution, and the spectral shifts of three different samples were measured for three times each. An inset graph in Fig. 4b shows the representative spectra measured from the DAS sensors treated with six different concentrations. As shown in Fig. 4b and its inset, the spectral shift was distinctly visible from the samples treated with 2×10^{-14} g of β-amyloid. The shift increased with the treated mass of β-amyloid and eventually saturated above 2×10^{-10} g. Therefore, the limit of measurement is about 20 femtogram and the dynamic range of measurement is about 4 orders of magnitude. Although active targeting of β-amyloid was not applied in this experiment, the present results clearly demonstrate that DAS can be utilized as a molecular sensor with femtogram-level sensitivity by accompanying suitable antibodies for target molecules. Furthermore, since the sensor size for measuring the absorbance curve with a conventional spectrophotometer is about 3 mm × 10 mm or less, the DAS fabricated on a 4-inch-scale substrate by the two simple steps of nanoimprinting and vacuum deposition yields more than 300 sensors.

Conclusions

In summary, we have presented a straightforward and high-throughput method for fabricating 3D plasmonic nanostructures on a flexible and transparent substrate. By depositing the Au film with a controlled oblique angle on a roll-to-roll nanoimprinted nanograting surface, it is possible to shape a plane film into an array of double-bent Au strips over a large area. The double-bent structure enables the lengthening of the oscillation path of surface plasmon in a limited space of a 200 nm-period grating, and consequently enhance the refractive index sensitivity as verified by experimental comparison with single-bent Au strips along with simulated charge distribution plots. Using the double-bent Au strips with a conventional spectrophotometer, consistent measurements of β-amyloid were demonstrated with femtogram-level sensitivity. The continuous roll-to-roll manufacturing methodology and straightforward working principle may spur the double-bent Au strip array to further extend its scalability and applicability; it can be conjugated with various antibodies on universal substrates, towards highly-sensitive, reliable, and inexpensive molecular detection platforms.

Acknowledgements

This research was supported by the Development of Platform Technology for Innovative Medical Measurements Program from the Korea Research Institute of Standards and Science (KRISS-2016-16011064), the National Research Foundation (NRF) grants (No. 2015M3A9D7029894, No. 2015R1A5A1037668, No. 2016R1C1B2016182, and 2016R1A2B4007858) funded by the Korean Government Ministry of Science, ICT & Future Planning (MISP), and Samsung Display, Co., Ltd.

References

1 K. A. Willets and R. P. Van Duyne, *Annu. Rev. Phys. Chem.*, 2007, **58**, 267.
2 J. N. Anker, W. P. Hall, O. Lyandres, N. C. Shah, J. Zhao and R. P. Van Duyne, *Nat. Mater.*, 2008, **7**, 442.
3 T. Ming, L. Zhao, Z. Yang, H. J. Chen, L. D. Sun, J. F. Wang and C. H. Yan, *Nano Lett.*, 2009, **9**, 3896.
4 W. S. Chang, J. W. Ha, L. S. Slaughter and S. Link, *Proc. Natl. Acad. Sci. U. S. A.*, 2010, **107**, 2781.
5 B. Luk'yanchuk, N. I. Zheludev, S. A. Maier, N. J. Halas, P. Nordlander, H. Giessen and C. T. Chong, *Nat. Mater.*, 2010, **9**, 707.
6 N. Verellen, P. Van Dorpe, C. J. Huang, K. Lodewijks, G. A. E. Vandenbosch, L. Lagae and V. V. Moshchalkov, *Nano Lett.*, 2011, **11**, 391.
7 A. E. Cetin and H. Altug, *ACS Nano*, 2012, **6**, 9989.
8 J. S. Wi, S. Tominaka and T. Nagao, *Adv. Opt. Mater.*, 2013, **1**, 814.
9 K. L. Lee, J. B. Huang, J. W. Chang, S. H. Wu and P. K. Wei, *Sci. Rep.*, 2015, **5**, 8547.
10 L. J. Guo, *Adv. Mater.*, 2007, **19**, 495.
11 J. G. Ok, Y. J. Shin, H. J. Park and L. J. Guo, *Appl. Phys. A: Mater. Sci. Process.*, 2015, **121**, 343.
12 S. H. Ahn and L. J. Guo, *Adv. Mater.*, 2008, **20**, 2044.
13 S. H. Ahn and L. J. Guo, *ACS Nano*, 2009, **3**, 2304.
14 J. G. Ok, H. S. Youn, M. K. Kwak, K. T. Lee, Y. J. Shin, L. J. Guo, A. Greenwald and Y. S. Liu, *Appl. Phys. Lett.*, 2012, **101**, 223102.
15 S. Koo, S. H. Lee, J. D. Kim, J. G. Hong, H. W. Baac, M. K. Kwak and J. G. Ok, *Int. J. Precis. Eng. Manuf.*, 2016, **17**, 943.
16 K. M. Mayer and H. H. Hafner, *Chem. Rev.*, 2011, **111**, 3828.
17 Y. Shen, J. Zhou, T. Liu, Y. Tao, R. Jiang, M. Liu, G. Xiao, J. Zhu, Z.-K. Zhou, X. Wang, C. Jin and J. Wang, *Nat. Commun.*, 2013, **4**, 2381.
18 F. Wu, L. Liu, L. Feng, D. Xu and N. Lu, *Nanoscale*, 2015, **7**, 13026.
19 M. M. Miller and A. A. Lazarides, *J. Phys. Chem. B*, 2005, **109**, 21556.
20 E. M. Larsson, J. Alegret, M. Kall and D. S. Sutherland, *Nano Lett.*, 2007, **7**, 1256.
21 E. Kazuma and T. Tatsuma, *Nanoscale*, 2014, **6**, 2397.
22 C. Haass and D. J. Selkoe, *Nat. Rev. Mol. Cell Biol.*, 2007, **8**, 101.
23 I. W. Hamley, *Chem. Rev.*, 2012, **112**, 5147.

